Structure-Properties Relationship in $RE_{3-x}Mg_xNi_9H_{10-13}$ (RE=La,Pr,Nd) Hydrides for Energy Storage

Volodymyr Yartys, Roman Denys

PII: S0925-8388(14)02951-X
DOI: http://dx.doi.org/10.1016/j.jallcom.2014.12.091
Reference: JALCOM 32824

To appear in: *Journal of Alloys and Compounds*

Please cite this article as: V. Yartys, R. Denys, Structure-Properties Relationship in $RE_{3-x}Mg_xNi_9H_{10-13}$ (RE=La,Pr,Nd) Hydrides for Energy Storage, *Journal of Alloys and Compounds* (2014), doi: http://dx.doi.org/10.1016/j.jallcom.2014.12.091

Structure-Properties Relationship in $RE_{3-x}Mg_xNi_9H_{10-13}$ (RE=La,Pr,Nd) Hydrides for Energy Storage

Volodymyr Yartys*[1,2] and Roman Denys[1]

[1] *Department of Energy Systems, Institute for Energy Technology, Kjeller, NO 2027, Norway*
[2] *Department of Materials Science and Engineering, Norwegian University of Science and Technology, Trondheim NO 7491, Norway*

* Corresponding author. Tel.: +47 454 22 065; e-mail: volodymyr.yartys@ife.no

ABSTRACT

Ternary $RE_{3-x}Mg_xNi_9$ intermetallics are promising battery electrode materials. Studies of the structure-properties relationships in the $(La,Pr,Nd)_{3-x}Mg_xNi_9H_{10-13}$ hydrides and initial intermetallics revealed the following: a) Increase of magnesium content causes a gradual shrinking of the trigonal unit cells (*a, c, V*) for all studied RE metals, with the highest solubility range of Mg reached in $REMg_2Ni_9$; b) Significant lowering of the thermodynamic stability follows an increase in magnesium content from x =1.0 to 1.1-1.2 and a replacement of La by Pr and Nd, with desorption pressures changing in a broad range, from 0.01 bar to 20 bar H_2; c) Neutron powder diffraction shows a nearly equal distribution of D atoms within the $REMgNi_4$ and $RENi_5$ layers; d) Local hydrogen ordering occurs within the H-sublattice built from MgH_6 octahedra and NiH_4 tetrahedra displaying a directional metal–hydrogen bonding. A partial substitution of Mg for RE allows the electrochemical discharge capacity of the $(La,Pr,Nd)_{3-x}Mg_xNi_9$ hydrides to become 25% greater than that of the commercial AB_5-type electrodes, reaching 400 mAh/g. Synthesis of the materials with a high degree of homogeneity is important and has been achieved by choosing an appropriate synthesis route, content of Mg in the initial mixtures, and time and temperature of the homogenisation process.

Keywords

Metal Hydrides / Magnesium / Neodymium / Nickel / Powder Neutron Diffraction / Crystal Structure

INTRODUCTION

Rechargeable Nickel–Metal Hydride (NiMH) batteries, originally developed for powering portable electronics, are now increasingly utilised in large-sized high power industrial applications, including Hybrid Electric Vehicles (HEV), high-power GIGACELL batteries by Kawasaki Heavy Industries for battery-driven light rail vehicles (LRV) and for the Battery Power System (BPS) for railway [1]. NiMH batteries offer significant advantages over the alternative secondary batteries, including excellent power densities, fast charge-discharge rates and long service life.

Metal hydride electrode serves as the negative electrode in the NiMH battery. Commercial MH battery electrodes utilise AB_5-type rare earth-based alloys (A is a battery grade mixture of rare earths (La,Ce,Pr,Nd) and B is nickel or a mixture of various transition metals and aluminium (Ni,Co,Mn,Al)). R&D activities aimed at the improvements of the electrochemical discharge capacity of AB_5, 320 mAh/g, and decrease of the price of the metal hydride battery alloys, recently shifted focus towards studies of a new family of the alloys composed of the AB_3- and A_2B_7-type rare earth-magnesium-based intermetallics [2].

In our work at the Institute for Energy Technology in Norway we have studied various aspects of the metal-hydrogen systems formed during substitution of La by Mg in $LaNi_3$ and La_2Ni_7 compounds [3-8]. This work included (a) Systematic studies of the influence of magnesium on the crystal structure and hydrogenation behaviour of the *PuNi*$_3$-type $La_{3-x}Mg_xNi_9$ (x = 0–2) intermetallic alloys [5]; (b) Neutron powder diffraction studies of the $La_2MgNi_9D_{13}$ deuteride, which witnessed local hydrogen ordering, with hydrogen sublattice built from the MgH_6 octahedra and NiH_4 tetrahedra [6]; (c) Probing the effect of magnesium content and quenching rate on the phase structure and composition of the rapidly solidified La_2MgNi_9 metal hydride battery electrode alloy [7]; (d) Investigations of the interrelation between the high temperature annealing and phase composition and electrochemical properties of the Co-free La_2MgNi_9 anode for the Ni-metal hydride batteries [8]; (e) Studies of the effect of La substitution by Nd on the phase-structural transformations in the RE_2MgNi_9–H_2 systems; and (f) *In situ* neutron powder diffraction studies of the charge-discharge processes in the metal hydride electrodes [9, 10].

The present paper focuses on studies of structure and thermodynamics of the $(La,Pr,Nd)_{3-x}Mg_xNi_9$ hydrides formed at various Mg/RE ratios for the light rare earth metals, La, Pr and Nd. *In situ* neutron powder diffraction and Pressure-Composition-Temperature diagrams were studied, yielding crystal structure data and thermodynamics of the formation-decomposition of the saturated hydrides $RE_2MgNi_9H(D)_{10-12}$. These data were complemented by studies of the electrochemical charge-discharge behaviours of $(La,Pr,Nd)_{3-x}Mg_xNi_9$ alloys as metal hydride anode materials.

EXPERIMENTAL

Arc melted pre-alloys (Nd-Ni, Pr-Ni, La-Nd-Ni) were crushed in a mortar and mixed with fine Mg powder (325 mesh, 99.8% pure). Mg was added with a 3 wt.% excess. In order to obtain a homogeneous distribution of the components, the powder mixture was ball milled in Ar atmosphere for up to 1 h (Fritsch P6; 80 ml vial; balls/powder=10:1; 150 rpm).

Milled powder was pressed under 5 ton/cm^2 into the pellets of 8 or 10 mm diameter. The pellets were placed into a Ta container, loaded into a stainless steel autoclave, filled with argon (1 bar; room temperature) and sealed. The heat treatment of the autoclaves was performed at 950°C for 6 hours, followed by a treatment at 800°C for 12 h. The autoclaves were quenched into cold water after the annealing.

In addition to the sintering, similar alloys were prepared by intermediate frequency induction melting under argon atmosphere from the starting element metals with a purity of not less than 99.5%. After induction melting, the melt was poured into a water-cooled copper mould. The alloy ingot was crushed and collected in a stainless steel cylindrical cell. The operation was done in an argon-filled glove box. Subsequently the cylindrical cell was placed into a furnace and the material was annealed at 950 °C for 6 h and water-quenched after the annealing.

Phase-structural analysis of the alloy was performed by X-ray powder diffraction using a Bruker D8 DISCOVER with a Ge-monochromator (Cu-Kα_1 radiation; λ=1.5406 Å) and a LYNX-Eye detector. The experimental data were processed using Rietveld profile refinements and GSAS software [11].

Hydrogen absorption-desorption properties of the alloys were characterized using a Sievert's type system. The samples were activated in vacuum at 250 °C for 30 min, cooled to 20 °C and then charged with a high purity hydrogen gas (99.999%). Pressure-composition-temperature (PCT) dependences of hydrogen absorption and desorption were measured on the activated sample at temperatures from 0 to 80 °C and H_2 pressures from 0.005 to 25 bar. In order to achieve activation, several complete hydrogen absorption–desorption cycles were performed prior to the PCT measurements to improve the kinetics of hydrogen exchange and to reach maximum hydrogen absorption capacities.

Electrochemical properties were tested in a three-electrode system with a 9 N KOH solution electrolyte at room temperature. A sintered $Ni(OH)_2$ electrode with a larger capacity than that of the MH electrode and an Hg/HgO (9 N KOH) electrode were used as the counter-electrode and reference electrode, respectively. The MH electrode was first activated at a 0.1 C rate for three charge–discharge cycles. Then, the rate capability and cycling stability were evaluated galvanostatically. The end potential of the discharge was set at −0.74 V vs. the Hg/HgO electrode.

In situ neutron diffraction studies of the Pr_2MgNi_9-, Nd_2MgNi_9- and $LaNdMgNi_9$-based deuterides were performed at the Spallation Neutron Source SINQ at Paul Scherrer Institute, Villigen, Switzerland, using a high resolution powder diffractometer HRPT in the high intensity mode (λ = 1.494 Å, 2θ range 4.05–164.9 °, step 0.05 °). The deuterides were synthesised in a cylindrical stainless steel container (wall thickness 0.2 mm, d_{inner}=6 mm), which was connected to a Sieverts' type apparatus and used as the sample cell during the *in situ* NPD experiments. The samples were charged with deuterium (98% purity) at 300 K and pressures from 10 to 18 bar ($La_2MgNi_9D_{13.1}$: 10 bar; $LaNdMgNi_9D_{12.5}$: 15.8 bar; $Pr_2MgNi_9D_{12}$: 17.4 bar; $Nd_2MgNi_9D_{12}$: 18 bar).

RESULTS

Initial alloys studied by X-Ray diffraction

Compounds with RE_2MgNi_9: stoichiometry - Pr_2MgNi_9 , Nd_2MgNi_9 and $LaNdMgNi_9$

Substitution of La in La_2MgNi_9 by Pr or Nd causes shrinking of the volumes of the unit cells by 2.2 % (Pr) and 2.6 % (Nd) (see Fig. 1) and yields materials with very similar properties. As expected, because of lanthanide contraction, the unit cell dimensions of Nd_2MgNi_9 (sp.gr. $R\bar{3}m$; a=4.9783(1), c=24.1865(9) Å; V=519.12(4) Å^3) are slightly lower, by 0.5-1.1 %, as compared to the isostructural intermetallic alloy La_2MgNi_9 (a=5.0314(2); c= 24.302(1) Å; V = 532.79(3) Å^3) [6]. $LaNdMgNi_9$ with equiatomic ratios between La, Nd and Mg, is closer to La_2MgNi_9 than to Nd_2MgNi_9, with the unit cell volume contracting by 1.2 % as compared to La_2MgNi_9.

A typical example of Nd_2MgNi_9 will be considered in more detail. Rietveld X-ray phase analysis showed formation of a nearly single phase alloy with a *$PuNi_3$* type intermetallic compound Nd_2MgNi_9 as a main constituent (>90 wt.%). Two minor secondary phases were observed in addition, $NdMgNi_4$ (*$MgCu_4Sn$* type; sp.gr. $F\bar{4}3m$; a=7.0917(3) Å) and $NdNi_5$ (*$CaCu_5$* type, sp.gr. *P6/mmm*; a=4.9606(7), c=3.9746(4) Å). Lattice parameters of impurity phases are in good agreement with the reference data, [12] and [13], respectively. The shortest interatomic Me-Me distances (Å) in the structure of Nd_2MgNi_9 are: Nd1...(Nd2/Mg), 3.548(5) Å; (Nd2/Mg)...(Nd2/Mg), 3.032(3) Å; Nd1...Ni, 2.8746(1) Å; (Nd2/Mg)...Ni, 2.907(6) Å; Ni...Ni, 2.431(8) Å.

Crystallographic data for the new compounds Pr_2MgNi_9, Nd_2MgNi_9 and $LaNdMgNi_9$ are listed in Table 1. Similar to the other characterised hybrid structures built from the stacking of the *$CaCu_5$* and Laves type layers, Mg exclusively occupies the Laves type layer, substituting half of Pr/Nd/(La,Nd) atoms in the 6*c* site. In contrast, no Pr/Nd/(La,Nd) substitution by Mg takes place within the *$CaCu_5$* layer (3*a* site), in agreement with the earlier reports for the $(RE,Mg)Ni_x$ hybrid structures.

Compounds $RE_{3-x}Mg_xNi_9$ (RE=La, Pr, Nd) with various RE/Mg ratios

The as cast $RE_{3-x}Mg_xNi_9$ (RE=La, Pr, Nd) alloys prepared by induction melting are multiphase and contain $RE_{3-x}Mg_xNi_9$, $(RE,Mg)_2Ni_7$, $REMgNi_4$ and $RENi_5$ intermetallics. SEM micrograph of a typical example (Fig. 2a; as cast $La_{2-x}Mg_{1+x}Ni_9$ alloy) shows that $RE_{3-x}Mg_xNi_9$ intermetallic has an abundance of around 50 %. However, an analysis of the SEM (Fig. 2b) and XRD (Fig. 3a) data showed formation of the trigonal $PuNi_3$ type intermetallics as the main constituents (>80%) for all $RE_{3-x}Mg_xNi_9$ alloys annealed at 950 °C.

In contrast to the alloys prepared via the induction melting, sintering of the precursor RE-Ni alloys and elementary Mg resulted in a significantly improved homogeneity of the materials, with the main component formed being $RE_{3-x}Mg_xNi_9$ intermetallic and with only minor amounts of impurity phases, including $RE_{1-x}Mg_xNi_2$, $RE_{2-x}Mg_xNi_7$, $RENi_5$ and $MgNi_2$, which were identified in some alloys. Formation of these impurities depends on the magnesium content of the alloys and is in agreement with the diagram of phase equilibria in the RE–Mg–Ni system. A

formation of a range of continuous solid solutions, $0 \leq x \leq 2.0$, reaching $REMg_2Ni_9$ takes place for RE = La and Nd. This is in agreement with previously reported formation of a continuous solid solution between the $LaNi_3$ and $LaMg_2Ni_9$ stoichiometries [5]. In the case of Pr, the highest Mg content in the studied samples was chosen as x = 1.2 and showed a formation of the $PuNi_3$ type alloy. Further studies are required to confirm the probable formation of $PrMg_2Ni_9$.

The compositions of the studied $RE_{3-x}Mg_xNi_9$ alloys (RE=La, Pr, Nd) and the corresponding crystal structure data obtained from the Rietveld refinements of high-resolution XRD data are listed in Tables 1 and 2. Crystallographic parameters for the $LaMg_2Ni_9$ and La_2MgNi_9 phases obtained in this work well agree with the published data [2,3] and [8], respectively. Because of the large differences in atomic radii (r_{Mg} = 1.602 Å vs. r_{La} = 1.897 Å; r_{Pr} = 1.81 Å; r_{Nd} = 1.79 Å), increase in the Mg/RE ratio leads to a continuous decrease of both unit cell parameters, *a* and *c*, and volumes of the unit cells (see Figure 1). RE substitution by Mg proceeds selectively, only inside the Laves-type slabs (6*c* site).

Hydrogenation properties. Thermodynamics and kinetics of interactions in the RE_2MgNi_9-H_2 (RE=La, Pr, Nd, La/Nd) systems

After activation by fast heating in dynamic vacuum to ~250°C, RE_2MgNi_9 easily absorbs hydrogen already during the first hydrogenation. At room temperature, a complete saturation of the alloys with hydrogen at a starting pressure of ~20 bar was reached within 15 min of interaction. Maximum hydrogen content of 12.2 and 13.3 at. H / f.u. RE_2MgNi_9 (RE = Nd and La) (H/M ~ 1.0) reached at these conditions, corresponds to ~1.5 wt.% H. On the second hydrogenation cycle, the hydrogenation rate becomes nearly two times faster (at room temperature of interaction) and it further increases with increasing temperature (reducing full hydrogenation time to ~2 min at 50-80°C). Maximum hydrogenation capacity of Nd_2MgNi_9 slightly increases at lower temperatures of the hydrogenation, approaching 13 at. H/f.u. at 0 °C and 20 bar H_2. Impurities give a minor contribution to the overall hydrogenation performance. Indeed, $PrNi_5$ and $NdNi_5$ remain nonhydrogenated as they absorb hydrogen at pressures exceeding 25 bar (room temperature) [13] which is above the pressure range used in the present work. On the other hand, at $P_{eq} \approx 1$ bar at 50°C $REMgNi_4$ form $REMgNiH_4$ hydrides containing appr. 0.67 at. H/M [12]. As the content of $REMgNi_4$ in the alloys is rather small (6 wt.% for Nd_2MgNi_9), its effect on the overall absorption-desorption characteristics is marginal.

PCT measurements showed that $RE_2MgNi_9H_{12-13}$ have a significantly lower thermodynamic stability as compared to $La_2MgNi_9H_{13}$. Similar to the La-based intermetallic, Pr_2MgNi_9, Nd_2MgNi_9 and $LaNdMgNi_9$ compounds show a single pressure plateau type P-C diagrams corresponding to a transformation from an α-solid solution of hydrogen in the intermetallic alloy to a β-hydride phase. However, as it is evident from the room temperature isotherms (Fig. 4a), equilibrium pressures of both hydrogen absorption and desorption in the Nd_2MgNi_9-H_2 system are an order of magnitude higher than in the La_2MgNi_9-H_2 system. Equilibrium hydrogen desorption pressure changes from <0.1 bar for the La_2MgNi_9-based hydride to >1 bar for $Nd_2MgNi_9H_{12}$.

Thermodynamic parameters of hydrogen desorption in the RE_2MgNi_9-H_2 systems (RE=Pr, Nd, La/Nd) were calculated from the van't Hoff dependencies of the midplateau pressures versus

reciprocal temperatures (Fig. 4b). Enthalpies of hydrogen desorption from the studied $RE_2MgNi_9H_{12-13}$ hydrides show variations ranging from 28.6(5) kJ/mol H_2 for $Nd_2MgNi_9H_{12}$ to 35.9(3) kJ/mol H_2 for $La_2MgNi_9H_{13}$.

Interestingly, some β-hydrides, including Nd_2MgNi_9-based β-phase have an extremely broad homogeneity range, with H content changing from ~8 to more than 12 at. H/f.u. This unusual feature of the Nd_2MgNi_9-H_2 system is a subject of our ongoing research.

A lower stability (higher formation/decomposition pressures) of Nd_2MgNi_9-based hydride can be explained by a smaller unit cell volume, which is lower by 2.7% as compared to $La_2MgNi_9H_{13}$. A similar correlation between the unit cell volumes of the intermetallic alloys and thermodynamic stability of the hydrides is a well-documented feature for the $RENi_5H_x$ hydrides (see e.g. [13]) and was also recently observed for the series of hydrogenated Mg-containing $La_{3-x}Mg_xNi_9$ (x=0–2) intermetallic alloys [5]. Changing of the Mg/La ratio in the $La_{3-x}Mg_xNi_9$ compounds allows one to achieve a huge variation of the hydride thermal stabilities. From the present study, it can be concluded that a partial substitution of La by Pr or Nd in the La_2MgNi_9 alloy allows to optimise the hydrogenation-dehydrogenation behaviours and to increase the rates of hydrogen exchange, allowing improvement of the electrochemical performance of the alloys as negative electrodes for the Ni-MH batteries.

Electrochemical studies of $RE_{3-x}Mg_xNi_9$ as battery anode materials

The hydrogen absorption–desorption behaviours and the electrochemical performance and electrochemical cycling stability of the $RE_{3-x}Mg_xNi_9$ alloys significantly improved after the annealing. The optimum discharge performance was demonstrated by the RE_2MgNi_9 alloys containing one Mg atom per formula unit. For the pellet electrodes, these annealed alloys had a discharge capacity of close to 400 mAh g^{-1} (see Fig. 5 giving representative examples for $LaNdMgNi_9$ and $La_{1.5}Nd_{0.5}MgNi_9$) as compared to 325 mAh g^{-1} for the as-cast sample. Replacement of La by Nd allows optimization of the electrochemical performance at high discharge currents. The discharge capacity of the annealed samples remained high, almost 50% after 300 cycles with 100% depth of discharge (DOD) in the half-cell tests.

Neutron powder diffraction study of the crystal structures of $RE_2MgNi_9D_{12-13}$ (RE=Pr, Nd, La/Nd). Structural similarities between the hydrides

The *in situ* NPD data for $RE_2MgNi_9D_{12}$ (RE=Pr, Nd, La/Nd) were collected at deuterium pressures of 10-18 bar at room temperature. Rietveld plots of the observed and calculated PND data for $Nd_2MgNi_9D_{12}$ deuteride are shown in Fig. 3b. Phase composition of the deuterated alloys correlates well with that of the initial alloys (See Fig. 3 where typical data are presented for Nd_2MgNi_9 and $Nd_2MgNi_9D_{12}$, as examples). In addition to the main $Nd_2MgNi_9D_{12}$ deuteride phase, small impurities of $NdNi_5$ and $NdMgNi_4D_4$ were also observed. The structure of the latter has been previously characterized by Guénée et al. [12] (sp.gr. *Pmn2₁*; *a*=5.0767(2), *b*=5.4743(2), *c*=7.3792(3) Å), and was used as a model in our Rietveld refinements. As already mentioned, $NdNi_5$ intermetallic does not form a hydride at the conditions applied in the present study.

The obtained structural data for the $RE_2MgNi_9D_{12}$ hydrides are presented in Table 3. Similar to $La_2MgNi_9H_{13}$ [6], formation of the $RE_2MgNi_9H_{12}$ hydrides proceeds via isotropic expansion of a trigonal unit cell ($\Delta a/a$=6.9-7.6%; $\Delta c/c$=9.4-9.6%; $\Delta V/V$=25.3-26.7 %).

D atoms partially occupy six, seven or eight types of interstitial positions in both Laves and $CaCu_5$-type slabs. Depopulation of one or two sites, as compared with $La_2MgNi_9D_{13}$ having 8 filled interstices, seems to be related to the volume of the unit cells. Indeed, for the smallest in volume $Nd_2MgNi_9D_{11.9}$ only six of eight sites remain occupied while for $LaNdMgNi_9D_{12.9}$ and $Pr_2MgNi_9D_{12.4}$ with intermediate between $Nd_2MgNi_9D_{11.9}$ and $La_2MgNi_9D_{13}$ unit cell volumes, the number of the filled sites becomes seven.

Formation of the hydrides is accompanied by isotropic volume expansion. $RE_2MgNi_9D_{12-13}$ is formed by filling of the existing interstitial sites. Volume expansion of the Laves- and $CaCu_5$-type slabs is very similar; ΔV_{RENi_5} =26.1-26.9 %, ΔV_{REMgNi_4} =24.6-26.6 %. Three occupied D-sites (D1, D2 and D4) are located within the $RENi_5$ slabs while three other sites (D5, D6 and D8) are within the $REMgNi_4$ slabs. In $Nd_2MgNi_9D_{12}$ from the overall stoichiometry of 12 at. D/f.u., 6.3(1) at. D are located inside the $NdNi_5$ slabs and 5.6(2) at. D/f.u. fill the $NdMgNi_4$ slabs. The calculated D content, $Nd_2MgNi_9D_{11.9(3)}$ ($NdNi_5D_{6.3(1)}$ + $NdMgNi_4D_{5.6(2)}$), agrees within the uncertainty with the value of 12.1(1) D/f.u. obtained from the volumetric measurements during synthesis of the deuteride. Very similar dependences are observed for $Pr_2MgNi_9D_{12}$ and $LaNdMgNi_9D_{12}$.

D atoms fill three types of tetrahedral interstices (D1: $RENi_3$; D2 and D8: Ni_4; D4: RE_2Ni_2). Furthermore, two D sites, D5 and D6, are located in the centres of trigonal bipyramids $(RE2/Mg)_3Ni_2$ and $RE1(RE2/Mg)_2Ni_2$ and have a triangular coordination $MgNi_2$. The conclusion stating such unusual coordination is based on the analysis of the distances between the metal and deuterium atomic positions. The mixed RE2/Mg site is randomly occupied by Mg and RE atoms in a 1:1 ratio. D5 and D6 sites are partially filled by D atoms with occupancies ≤50%. The distances from RE2/Mg 6*c* site to the D5 and D6 sites are 1.91(1) and 1.97(2) Å, respectively. Apparently, both values are too short for the large Nd atom (r_{Nd}=1.82 Å) to assume their filling with hydrogen atoms; in contrast, they are in the same range as Mg–D bond lengths in the structures of α- and γ-MgD_2 binary hydrides, 1.9-2.0 Å [17]. Thus, D5 and D6 positions can be only occupied in a case when they have Mg atoms (r_{Mg}=1.60 Å) in their nearest surrounding. The minimum distance between Nd and D atoms in the structure is 2.3 Å, while Ni−D distances are within a range from 1.51 to 1.76 Å.

Comparison of the metal-metal distances in the structures of the initial compound and its hydride shows that these distances change quite significantly, by an 8% increase on average on hydrogenation. The most pronounced expansion is observed in the coordination sphere of the Ni3 atoms.

Analysis of the neutron scattering data for $Nd_2MgNi_9D_{12}$ and $La_2MgNi_9D_{13}$ indicates that the Mg-H and Ni-H distances are very close to each other in both structures and that a local hydrogen ordering takes place in the hydride, with hydrogen sublattice being built from the MgH_6 octahedra and NiH_4 tetrahedra (see Fig. 6, a and b).

Such local hydrogen ordering within the H-sublattice was firstly observed in the structure of $La_2MgNi_9H_{13}$ deuteride. The number of hydrogen-filled sites in the Pr- and Nd-containing hydrides (6 or 7) is decreased as compared to 8 occupied sites in $La_2MgNi_9H_{13}$; however, a decrease in the number of the filled sites does not change the local ordering of hydrogen in the hydride structures.

The stacking of the MgH_6 octahedra and NiH_4 tetrahedra stabilises the structures and manifests a directional bonding between the metal (Mg and Ni) and hydrogen atoms.

CONCLUDING REMARKS

This study shows that $RE_{3-x}Mg_xNi_9$ intermetallics are promising materials for energy storage applications, particularly as efficient anodes of the rechargeable Ni-Metal Hydride batteries. Their properties are very much influenced by the degree of the homogeneity of the materials, and appropriate synthesis routes should be applied to optimise content of Mg in the initial mixtures, time and temperature of the homogenisation process. For optimal materials, a partial substitution of Mg for RE and, also, of La for Nd and Pr, allows the electrochemical discharge capacity of the $(La,Pr,Nd)_{3-x}Mg_xNi_9$ hydrides to reach 400 mAh/g and remain high, almost 50% after 300 cycles with 100% depth of discharge (DOD). Significant lowering of the thermodynamic stability follows an increase in magnesium content from x =1.0 to 1.1-1.2 and a replacement of La by Pr and Nd, with desorption pressures changing in a broad range, from 0.01 bar to 20 bar H_2;

In situ neutron diffraction studies of the structure-properties relationships in the initial intermetallics and their corresponding saturated $(La,Pr,Nd)_{3-x}Mg_xNi_9H_{10-13}$ hydrides revealed the following:

a) An increase of magnesium content causes gradual shrinking of the trigonal unit cells (*a*, *c*, *V*) for all studied RE metals, with the highest solubility range of Mg reached in $REMg_2Ni_9$;
b) Neutron powder diffraction showed a nearly equal distribution of D atoms within the $REMgNi_4$ and $RENi_5$ layers;
c) Local hydrogen ordering occurs within the H-sublattice built from MgH_6 octahedra and NiH_4 tetrahedra, displaying a directional metal–hydrogen bonding.

Further work should be done to develop the alloys characterised by fast rates of hydrogen exchange, allowing the achievement of advanced performance of metal hydride batteries at high discharge current densities.

ACKNOWLEDGEMENTS

The research activities were funded by the projects NOVELMAG (FP7, M.Era-RUS program, project # 225) and “Novel Mg-based materials for advanced Ni-Metal Hydride batteries” (program NANOMAT; project # 203323 of the Research Council of Norway).
We are grateful to Dr. Christopher Nwakwuo (NTNU and IFE), Dr. Wei-Kang Hu (IFE), Dr. Alexey Volodin (IPChPh RAS and IFE), Dr. Michel Latroche and Dr. Fermin Cuevas (both

ICMPE, CNRS, France) for the fruitful collaboration on various aspects of studies of the magnesium-containing materials for energy storage.

REFERENCES

[1] T.Takasaki, K. Nishimura, H.Fukunaga, T. Iwaki, T. Sakai. Development of Cobalt- free RE-Mg-Ni alloy (RE: rare earth) for large-sized Nickel-metal hydride battery.// International Symposium on Metal-Hydrogen Systems MH2012. Kyoto, Japan, 2012. WeOA07. Collected Abstracts, p.317.

[2] Y. Liu, Y. Cao, L. Huang, M. Gao, H. Pan. Rare earth–Mg–Ni-based hydrogen storage alloys as negative electrode materials for Ni/MH batteries *J. Alloys Compd.* 509 (3) (2011) 675-686.

[3] R.V. Denys, A.B. Riabov, V.A. Yartys, R.G. Delaplane, M. Sato. Hydrogen storage properties and structure of $La_{1-x}Mg_x(Ni_{1-y}Mn_y)_3$ intermetallics and their hydrides. *J. Alloys Compd.* 446–447 (2007) 166-172.

[4] R.V. Denys, A.B. Riabov, V.A. Yartys, M. Sato, R.G. Delaplane. Mg substitution effect on the hydrogenation behaviour, thermodynamic and structural properties of the La_2Ni_7–$H(D)_2$ system. *J. Solid State Chem.* 181(4) (2008) 812-821.

[5] R.V. Denys, V.A. Yartys. Effect of magnesium on crystal structure and thermodynamics of the $La_{3-x}Mg_xNi_9$ hydrides. *J. Alloys Compd.* 509 (Suppl.2) (2011) S540-S548.

[6] R.V. Denys, V.A. Yartys, C.J. Webb. Hydrogen in $La_2MgNi_9D_{13}$. The role of magnesium. *Inorg. Chem.* 51 (2012) 4231-4238.

[7] C.C. Nwakwuo, T. Holm, R.V. Denys, W. Hu, J.P. Maehlen, J.K. Solberg, V.A. Yartys. Effect of magnesium content and quenching rate on the phase structure and composition of rapidly solidified La_2MgNi_9 metal hydride battery electrode alloy. *J. Alloys Compd.* 555 (2013) 201-208.

[8] W. Hu, R.V. Denys, C.C. Nwakwuo, T. Holm, J.P. Maehlen, J. K. Solberg, V.A. Yartys. Annealing effect on phase composition and electrochemical properties of the Co-free La_2MgNi_9 anode for Ni-Metal Hydride batteries. *Electrochimica Acta* 96 (2013) 27–33.

[9] A.B. Riabov, M. Latroche, F. Cuevas, R.V. Denys, Weikang Hu, V.A. Yartys. *In situ* PND studies of deuterium absorption-desorption in the La_2MgNi_9 metal hydride battery alloy.*Abstr. Int. Symp. Metal-Hydrogen Systems* (*MH2012*), Kyoto, Japan, 2012. p. 421.

[10] Michel Latroche, Fermìn Cuevas, Wei-Kang Hu, Denys Sheptyakov, Roman V. Denys and Volodymyr A. Yartys. Mechanistic and kinetic study of the electrochemical charge and discharge of La_2MgNi_9 by in situ powder neutron diffraction.// *J. Phys. Chem. C*, **2014**, *118* (23), pp 12162–12169.

[11] A.C. Larson, R.B.V. Dreele, *General Structure Analysis System (GSAS)*, in: Los Alamos National Laboratory Report LAUR, 2000, pp. 86–748.

[12] L. Guénée, V. Favre-Nicolin, K. Yvon. Synthesis, crystal structure and hydrogenation properties of the ternary compounds $LaNi_4Mg$ and $NdNi_4Mg$. *J. Alloys Compd.* 348 (2003) 129–137.

[13] H. Senoh, N. Takeichi, H. T. Takeshita, H. Tanaka, T. Kiyobayashi and N. Kuriyama. Hydrogenation and Dehydrogenation Properties of R_HNi_5 (R_H = Heavy Rare Earth) Binary Intermetallic Compounds. *Mater. Trans.* 44 (9) (2003) 1663–1666.

[14] C.C. Nwakwuo, V.A. Yartys et al. SEM microstuctural study of the $RE_{3-x}Mg_xNi_9$ (RE=La, Pr, Nd) alloys. In preparation for publication in *J. Alloys Compd.*

[15] Roman V. Denys, Volodymyr A. Yartys , Colin J. Webb. $LaNi_5$-assisted hydrogenation of $MgNi_2$ in the hybrid structure of $LaMg_2Ni_9D_{9.5}$.// MH2012, Kyoto, Japan, 21-26 October 2012. Poster presentation. MoP38. Collected Abstracts. P.92.

[16] A.A.Volodin, R.V. Denys, G.A.Tsirlina, B.P. Tarasov, M. Fichtner, V.A.Yartys. Hydrogen Diffusion in $La_{1.5}Nd_{0.5}MgNi_9$ Alloy Electrodes of the Ni/MH Battery.// Proceedings of the MH2014. Submitted to *J. Alloys Compd.* and 14th International Symposium on Metal-Hydrogen Systems. Fundamentals and Applications. 20-25 July 2014. Manchester, U.K. Collected Abstracts. p.350.

[17] M. Bortz, B. Bertheville, G. Bottger, K. Yvon. Structure of the high pressure phase γ-MgH_2 by neutron powder diffraction. *J. Alloys Compd.* 287 (1999) L4–L6.

Figure captions in the manuscript

Structure-Properties Relationship in $RE_{3-x}Mg_xNi_9H_{10-13}$
(RE=La,Pr,Nd) Hydrides for Energy Storage
by
Volodymyr Yartys and Roman Denys

Figure 1. Metrics of the unit cells of the $La_{3-x}Mg_xNi_9$, $Pr_{3-x}Mg_xNi_9$ and $Nd_{3-x}Mg_xNi_9$ (x=0-2.1) intermetallics as related to the magnesium content.

Figure 2. Scanning electron microscopy micrographs for the as cast (a) and annealed at 950 °C for 6 h (b) $La_{2-x}Mg_{1+x}Ni_9$ alloy showing typical changed of phase-structural composition [14]. The as cast alloy contains $La_{3-x}Mg_xNi_9$, $(La,Mg)_2Ni_7$, $LaMgNi_4$ and $LaNi_5$ intermetallics. Annealing at 950 °C results in the alloy containing $La_{3-x}Mg_xNi_9$ and $(La,Mg)_2Ni_7$ and eliminating $LaMgNi_4$ and $LaNi_5$.

Figure 3. X-ray diffraction pattern of Nd_2MgNi_9 alloy (a) and in situ neutron diffraction pattern of $Nd_2MgNi_9D_{12}$ deuteride (b).

Figure 4. PCT diagrams (a) and van't Hoff plots (b) for Nd_2MgNi_9-H_2, Pr_2MgNi_9-H_2 and La_2MgNi_9–H_2 systems.

Figure 5. Discharge curves for RE_2MgNi_9-based metal hydride anodes at a current density 60mA g^{-1}.

Figure 6. Local ordering of deuterium in the crystal structures of $RE_2MgNi_9D_{12-13}$ showing formation of MgD_6 octahedra and NiD_4 tetrahedra (a) and their packing (b).

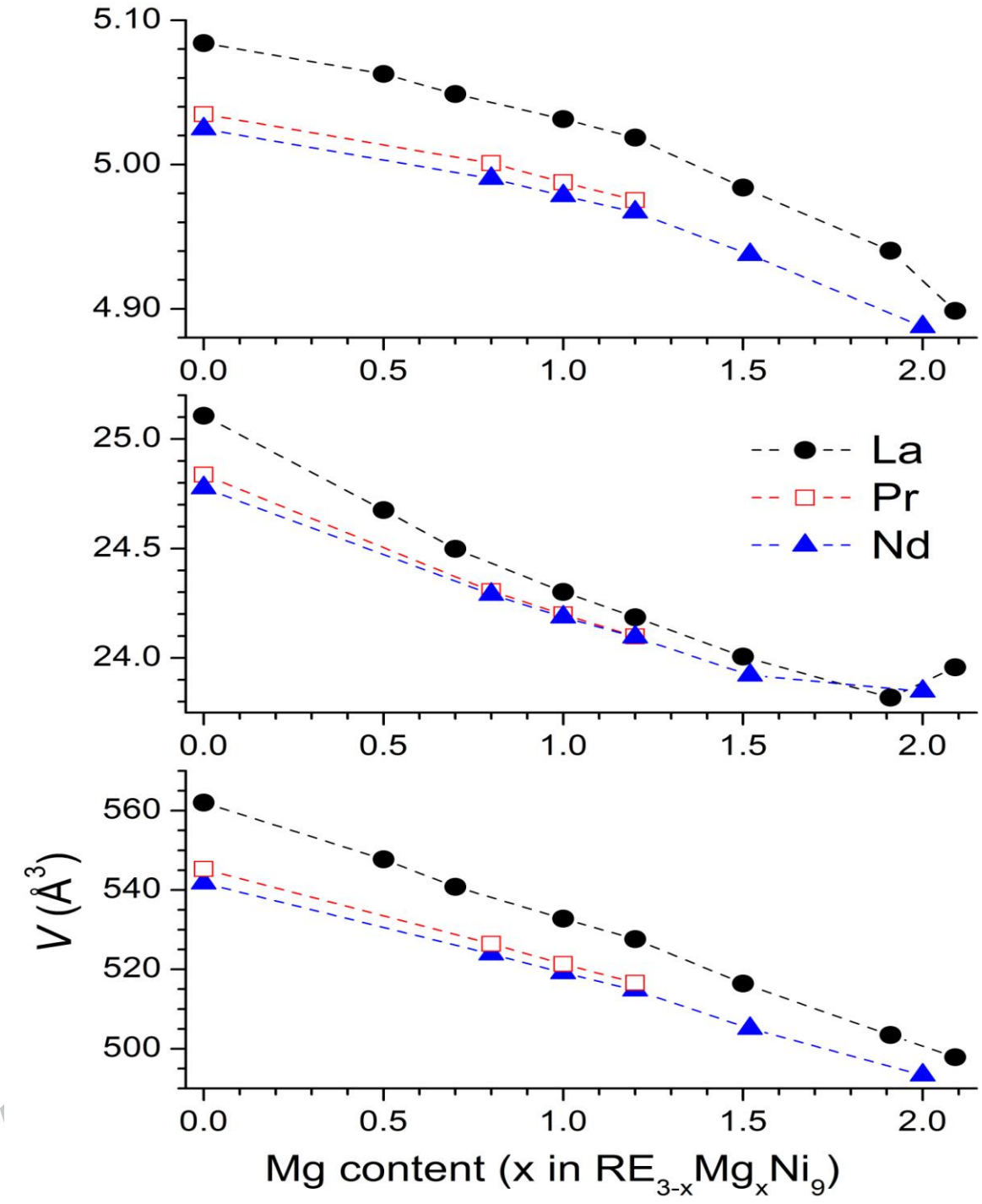

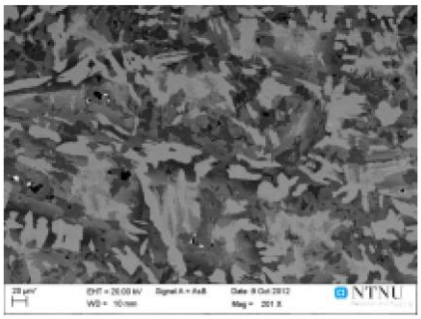

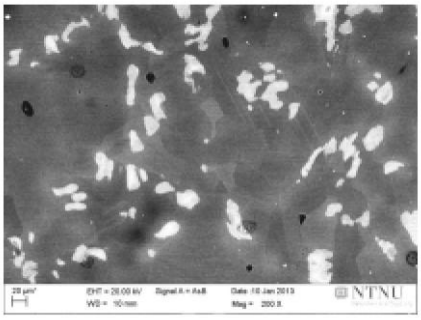

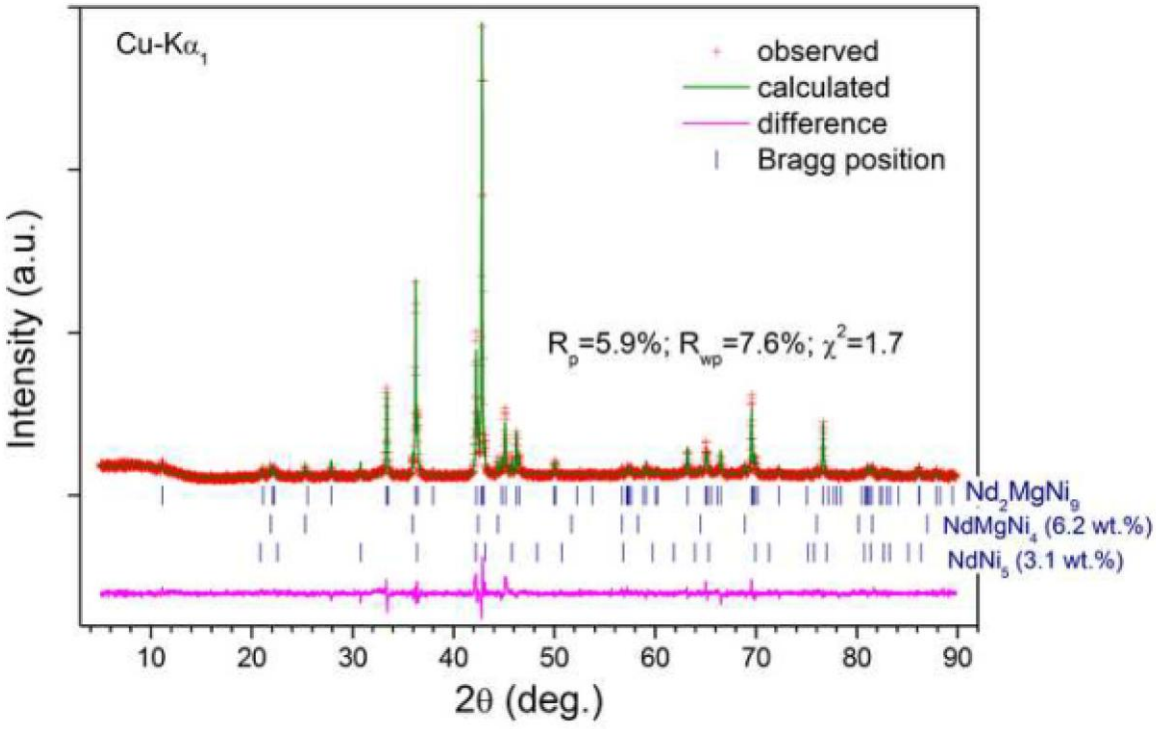

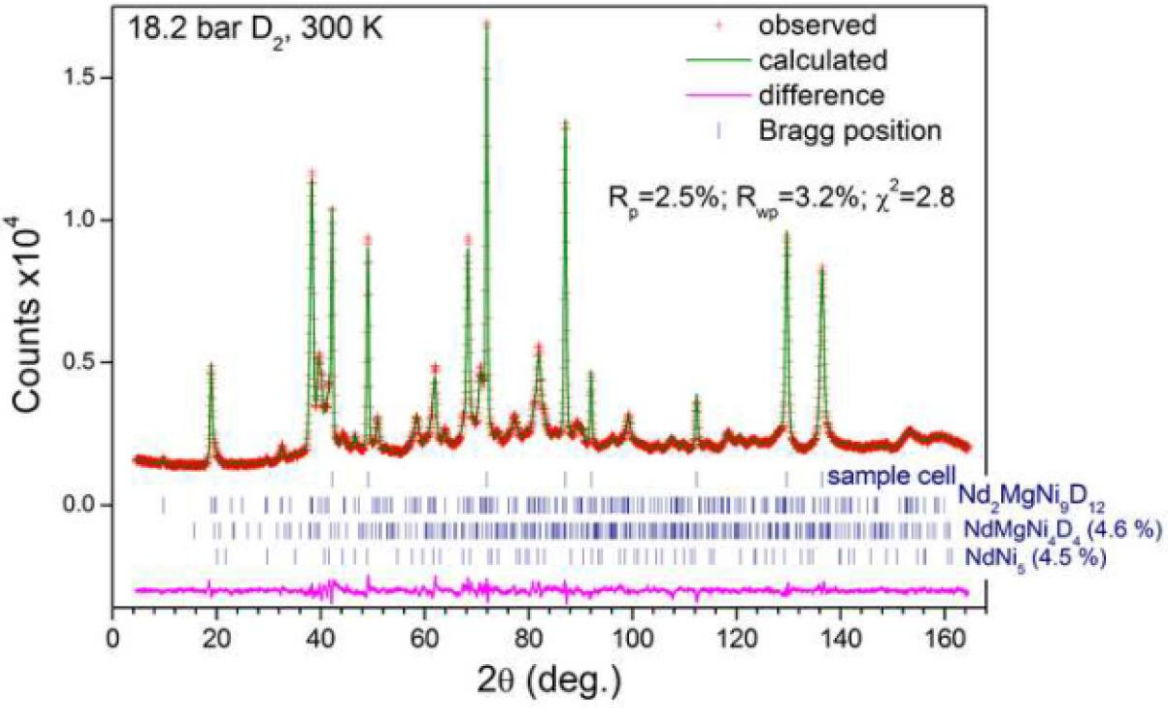

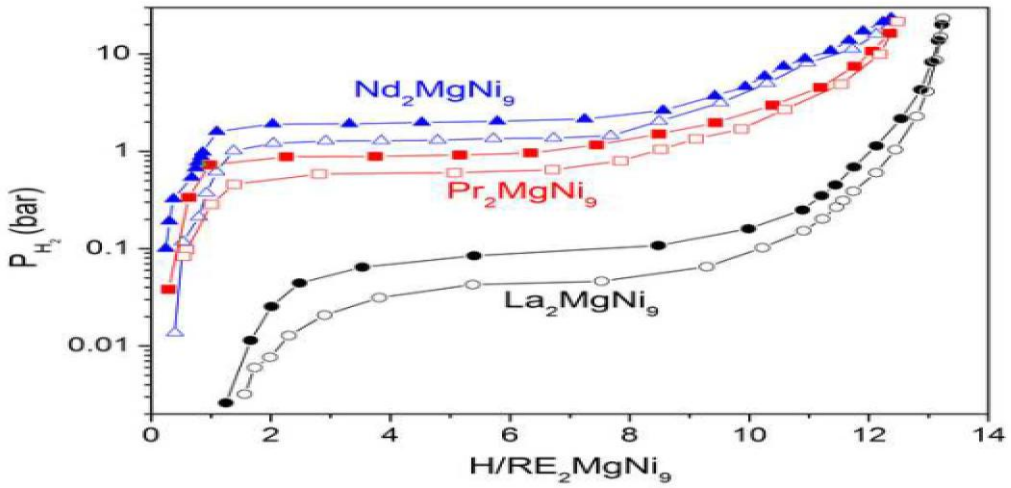

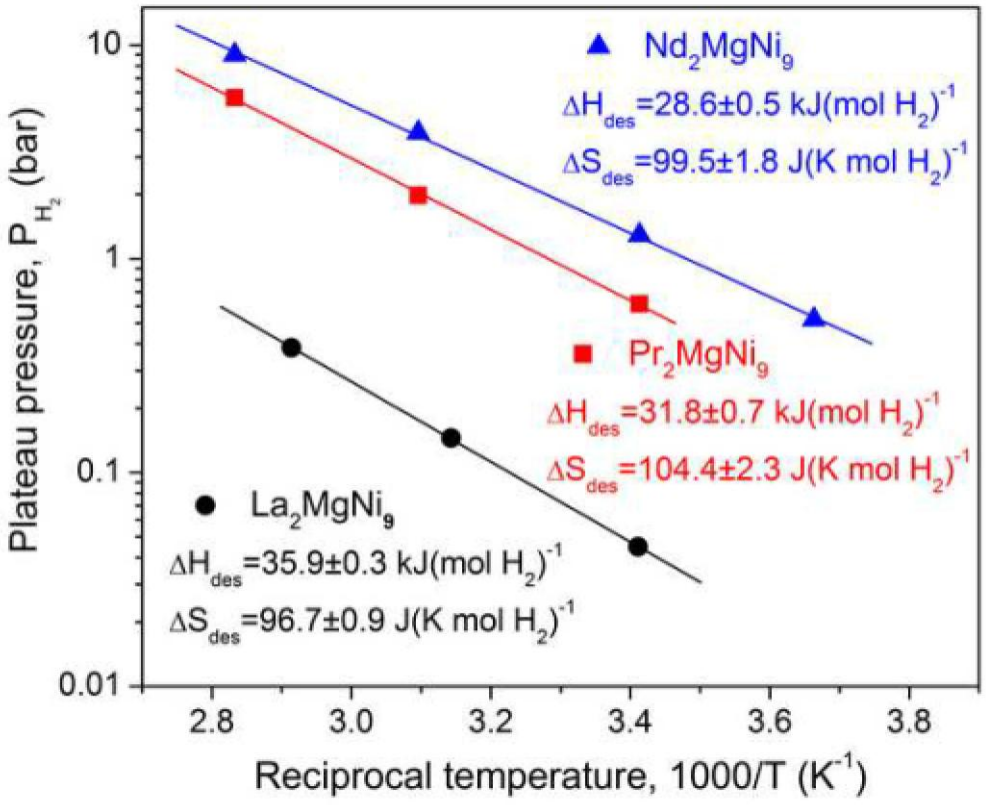

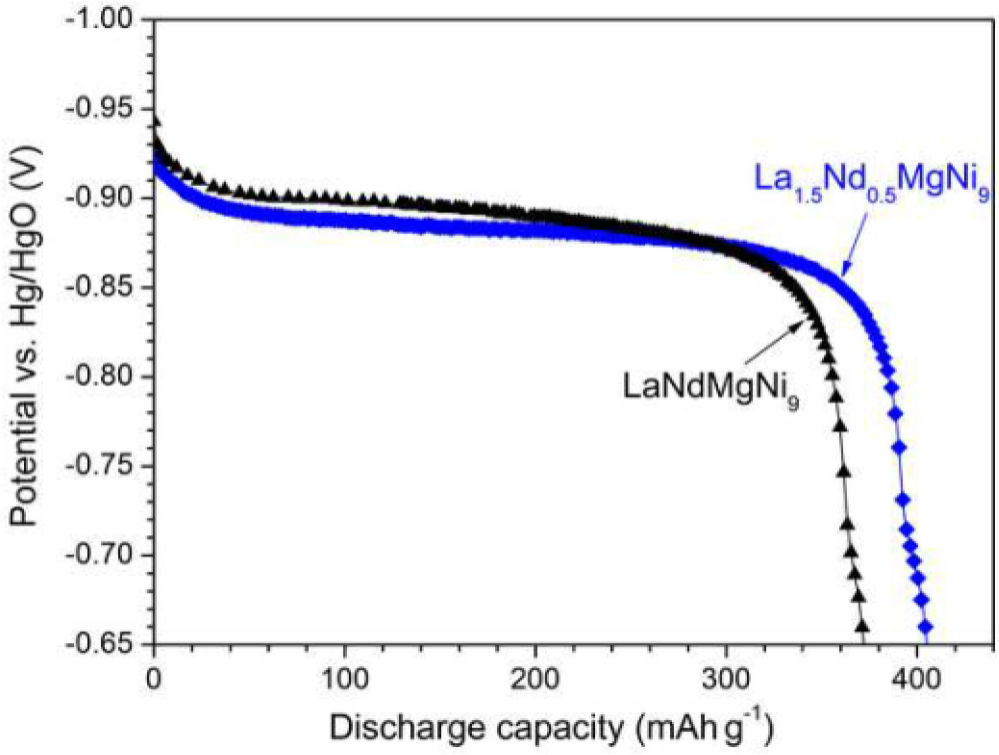

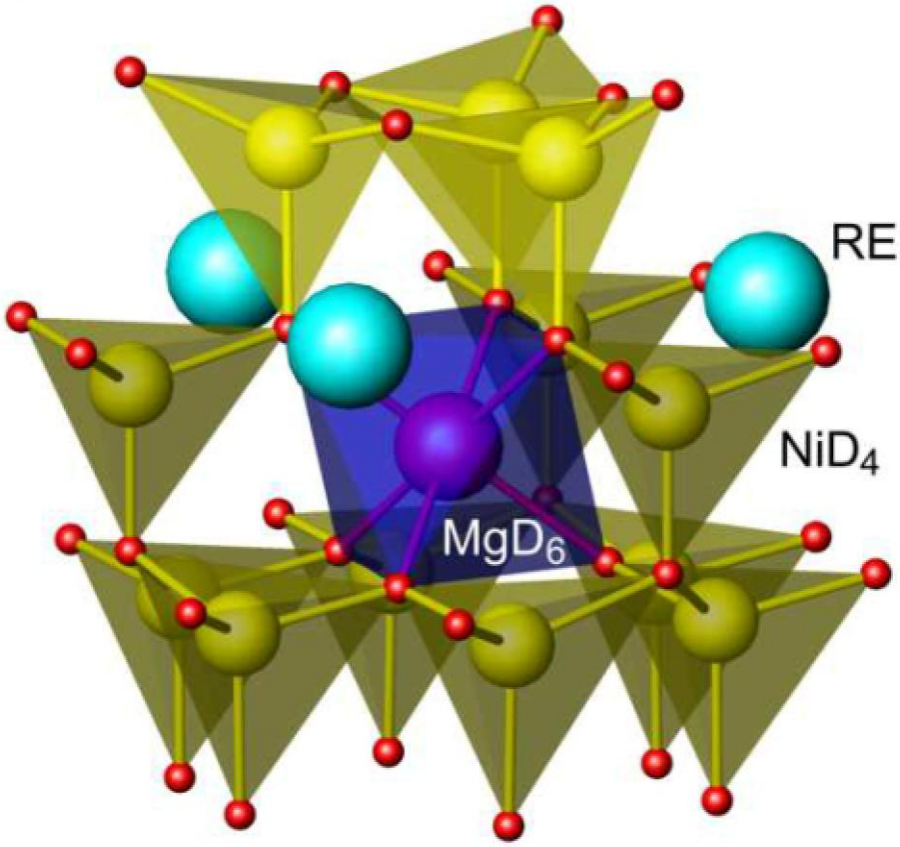

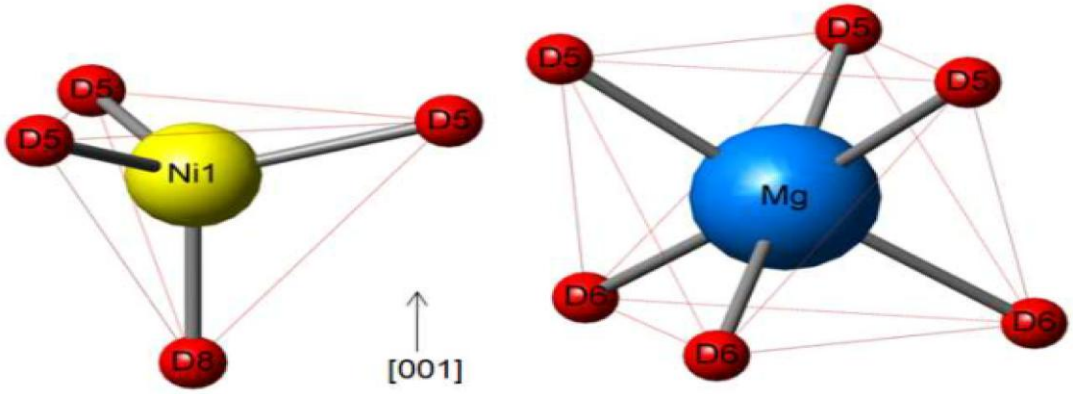

$La_2MgNi_9D_{13}$: $\delta_{(Ni1\text{-}D)}$ = 1.52 Å; $\delta_{(Mg\text{-}D)}$ =1.97-2.03 Å

$Pr_2MgNi_9D_{12}$: $\delta_{(Ni1\text{-}D)}$ = 1.52-1.62 Å; $\delta_{(Mg\text{-}D)}$ =1.91-2.02 Å

$Nd_2MgNi_9D_{12}$: $\delta_{(Ni1\text{-}D)}$ = 1.51-1.63 Å; $\delta_{(Mg\text{-}D)}$ =1.91-1.97 Å

Highlights in the paper

Structure-Properties Relationship in $RE_{3-x}Mg_xNi_9H_{10-13}$
(RE=La,Pr,Nd) Hydrides for Energy Storage

by

Volodymyr Yartys and Roman Denys

- Increase of Mg content in the $RE_{3-x}Mg_xNi_9$ causes gradual shrinking of the cells
- The highest solubility range of Mg in $RENi_3$ is $REMg_2Ni_9$
- An increase in Mg, Pr and Nd content reduces stability of the hydrides
- NPD showed a nearly equal distribution of D within the Laves and $RENi_5$ type layers
- H-sublattice is locally ordered ad contains MgH_6 octahedra and NiH_4 tetrahedra

Table 1

Unit cell parameters of the $RE_{3-x}Mg_xNi_9$ intermetallics (*PuNi*$_3$ type, Sp.gr. $R\bar{3}m$).

Alloy	*a*, Å	*c*, Å	*V*, Å^3	*c*/*a*	Ref.
$LaNi_3$	5.0842(2)	25.106(1)	562.03(4)	4.94	[5]
$La_{2.5}Mg_{0.5}Ni_9$	5.06276(7)	24.6752(4)	547.73(1)	4.87	[5]
$La_{2.3}Mg_{0.7}Ni_9$	5.0488(2)	24.498(1)	540.80(3)	4.85	[5]
La_2MgNi_9	5.0314(2)	24.302(1)	532.79(3)	4.83	[5, 6]
$La_{1.5}Mg_{1.5}Ni_9$	4.9840(2)	24.006(1)	516.41(3)	4.82	[5]
$La_{1.09}Mg_{1.91}Ni_9$	4.94024(8)	23.8188(4)	503.44(1)	4.82	[15]
$La_{0.91}Mg_{2.09}Ni_9$	4.8986(1)	23.957(1)	497.86(2)	4.89	[15]
$PrNi_3$	5.0349(1)	24.837(1)	545.28(2)	4.93	this work
$Pr_{2.2}Mg_{0.8}Ni_9$	5.0009(1)	24.305(1)	526.41(3)	4.86	this work
Pr_2MgNi_9	4.9877(1)	24.1988(8)	521.35(4)	4.85	this work
$Pr_{1.8}Mg_{1.2}Ni_9$	4.9753(1)	24.0978(6)	516.58(3)	4.84	this work
$NdNi_3$	5.0246(3)	24.777(2)	541.73(10)	4.93	this work
$Nd_{2.2}Mg_{0.8}Ni_9$	4.9902(2)	24.290(2)	523.86(6)	4.87	this work
Nd_2MgNi_9	4.9783(1)	24.1865(9)	519.12(4)	4.86	this work
$Nd_{1.8}Mg_{1.2}Ni_9$	4.9670(1)	24.0949(7)	514.80(3)	4.85	this work
$Nd_{1.5}Mg_{1.5}Ni_9$	4.9375(1)	23.9210(7)	505.04(3)	4.84	this work
$NdMg_2Ni_9$	4.8875(1)	23.8477(7)	493.34(1)	4.88	this work
$LaNdMgNi_9$	5.0066(2)	24.239(1)	526.18(4)	4.84	this work
$La_{1.5}Nd_{0.5}MgNi_9$	5.0258(1)	24.305(1)	531.66(3)	4.84	[16]

Table 2

Atomic parameters of RE_2MgNi_9 compounds (*$PuNi_3$* type, sp. gr. $R\bar{3}m$) from Rietveld refinements of X-ray diffraction data.

Atom	La_2MgNi_9 [1]	Pr_2MgNi_9	Nd_2MgNi_9	$LaNdMgNi_9$
RE1 in 3*a* (0, 0, 0) U_{iso}×100 (Å2)	1.1(1)	2.2(1)	2.3(1)	0.9(2)
RE2/Mg in 6c (0, 0, *z*) *z* U_{iso}×100 (Å^2) n_{Mg}, (n_{RE}=1–n_{Mg})	0.1430(2) 1.3(1) 0.5(1)	0.1459(2) 1.3(1) 0.492(8)	0.1467(2) 1.6(2) 0.491(5)	0.1434(2) 1.5(2) 0.491(5)
Ni1 in 3*b* (0, 0, ½) U_{iso}×100 (Å^2)	0.2(1)	0.9(1)	0.3(1)	0.5(–)
Ni2 in 6*c* (0, 0, *z*) *z* U_{iso}×100 (Å^2)	0.3318(3) 0.7(2)	0.3308(3) 0.9(1)	0.3315(3) 0.3(1)	0.3323(3) 0.5(–)
Ni3 in 18*h* (*x*, –*x*, *z*) *x* *z* U_{iso}×100 (Å^2)	0.4994(6) 0.0831(2) 0.67(9)	0.4987(5) 0.0824(2) 0.9(1)	0.4985(5) 0.0825(2) 0.3(1)	0.5004(5) 0.0835(2) 0.5(–)
R-factors R_p R_{wp} χ^2	 13.2 17.4 1.9	 6.1 7.9 1.7	 5.9 7.6 1.7	 7.2 9.1 1.3
Impurity phases	6.8 wt% $LaMgNi_4$	1.7 wt% $PrNi_5$ 0.6 wt% $PrMgNi_4$	3.1 wt% $PrNi_5$ 6.2 wt% $PrMgNi_4$	4.6 wt% $RENi_5$ 5.4 wt% $REMgNi_4$

Table 3

Unit cell dimensions of the $RE_2MgNi_9D_{\sim 12}$ deuterides (sp. gr. $R\bar{3}m$) from Rietveld refinements of the in situ powder neutron diffraction data collected at 300 K.

Deuteride	$P(D_2)$, bar	a, Å	c, Å	V, Å^3	$\Delta a/a$, %	$\Delta c/c$, %	$\Delta V/V$, %	$\Delta V(AB_5)$, %	$\Delta V(AB_2)$, %,
$La_2MgNi_9D_{13}$	10.2	5.4151(1)	26.584(2)	675.10(6)	7.6	9.4	26.7	26.9	26.6
$LaNdMgNi_9D_{12.9}$	15.8	5.3672(1)	26.602(2)	663.65(5)	7.2	9.7	26.1	26.0	26.3
$Pr_2MgNi_9D_{12.4}$	17.4	5.3447(2)	26.512(2)	655.87(6)	7.2	9.6	25.8	26.7	24.9
$Nd_2MgNi_9D_{11.9}$	18.2	5.3236(2)	26.506(2)	650.55(7)	6.9	9.6	25.3	26.1	24.6

Table 4

Atomic parameters of the $RE_2MgNi_9D_{\sim 12}$ deuterides (*PuNi*$_3$ type, sp. gr. $R\bar{3}m$) from Rietveld refinements of X-ray diffraction data

Atom	$La_2MgNi_9D_{13}$ [2]	$LaNdMgNi_9D_{12.9}$	$Pr_2MgNi_9D_{12.4}$	$Nd_2MgNi_9D_{11.9}$
RE1 in 3*a* (0, 0, 0)				
U_{iso}×100 (Å2)	3.4(2)	0.6(3)	0.7(3)	1.3(2)
RE2/Mg in 6c (0, 0, *z*)				
z	0.1468(4)	0.1408(3)	0.1409(4)	0.1405(4)
U_{iso}×100 (Å^2)	3.7(2)	2.6(2)	3.7(3)	2.8(2)
n_{Mg}, (n_{RE}=1–n_{Mg})	0.5(–)	0.5(–)	0.5(–)	0.5(–)
Ni1 in 3*b* (0, 0, ½)				
U_{iso}×100 (Å^2)	2.2(2)	1.1(2)	2.3(2)	2.5(2)
Ni2 in 6*c* (0, 0, *z*)				
z	0.3318(3)	0.3285(2)	0.3274(2)	0.3278(2)
U_{iso}×100 (Å^2)	2.1(2)	1.5(1)	1.9(1)	1.5(1)
Ni3 in 18*h* (*x*, –*x*, *z*)				
x	0.4967(4)	0.4982(5)	0.4979(4)	0.4966(4)
z	0.0832(1)	0.0834(1)	0.0830(1)	0.0830(1)
U_{iso}×100 (Å^2)	1.34(4)	1.02(4)	1.27(3)	1.21(6)
D1	18*h* (*x*, –*x*, *z*)	36*i* (*x*, y, *z*)	36*i* (*x*, y, *z*)	36*i* (*x*, y, *z*)
x	0.494(2)	0.538(3)	0.530(3)	0.537(3)
y	–*x*	0.544(3)	0.555(2)	0.553(2)
z	0.0196(4)	0.0166(4)	0.0191(4)	0.0189(4)
n	0.395(6)	0.233(4)	0.243(5)	0.239(4)
D2 in 6*c* (0, 0, *z*)				
z	0.390(1)	0.3889(8)	0.3853(8)	0.3907(9)
n	0.28(1)	0.30(1)	0.33(1)	0.31(1)
D3 in 18*h* (*x*, –*x*, *z*)				
x	0.145(4)	0.182(5)	0.170(4)	–
z	0.084(1)	0.0702(5)	0.087(1)	–
n	0.17(1)	0.133(9)	0.13(1)	–
D4 in 18*h* (*x*, –*x*, *z*)				
x	0.854(1)	0.848(1)	0.851(1)	0.851(2)
z	0.0843(4)	0.0704(5)	0.0734(4)	0.0710(5)
n	0.584(8)	0.49(1)	0.48(1)	0.47(1)
D5 in 18*h* (*x*, –*x*, *z*)				
x	0.4868(9)	0.496(1)	0.501(1)	0.502(1)
z	0.1485(3)	0.1483(3)	0.1494(3)	0.1493(3)
n	0.499(5)	0.487(7)	0.45(1)	0.476(7)
D6 in 18*h* (*x*, –*x*, *z*)				
x	0.798(2)	0.829(2)	0.811(2)	0.820(2)
z	0.1191(8)	0.0989(6)	0.1032(7)	0.1001(6)
n	0.25(1)	0.34(1)	0.29(1)	0.34(1)
D7 in 6*c* (0, 0, *z*)				
z	0.235(4)	–	–	–
n	0.12(1)	–	–	–
D8 in 6*c* (0, 0, *z*)				
z	0.4429(5)	0.4424(6)	0.4429(6)	0.4431(8)
n	0.45(2)	0.40(2)	0.38(2)	0.33(2)
U_{iso}×100 (Å^2) for D1-D8	1.99(8)	2.32(9)	2.5(1)	2.4(1)
R-factors:				
R_p	2.5	2.8	2.8	2.5
R_{wp}	3.3	3.8	3.7	3.2
χ^2	9.3	8.3	3.7	2.8
calculated D content	13.1(1)	12.9(1)	12.4(2)	11.9(1)
volumetric data	13.0	13.0	12.5	12.1